Lab on a Chip

PAPER

View Article Online
View Journal | View Issue

Cite this: *Lab Chip*, 2015, **15**, 417

Microfluidic system for high throughput characterisation of echogenic particles†

Paul Rademeyer, Dario Carugo, Jeong Yu Lee and Eleanor Stride*

Received 13th October 2014,
Accepted 28th October 2014

DOI: 10.1039/c4lc01206b

www.rsc.org/loc

Echogenic particles, such as microbubbles and volatile liquid micro/nano droplets, have shown considerable potential in a variety of clinical diagnostic and therapeutic applications. The accurate prediction of their response to ultrasound excitation is however extremely challenging, and this has hindered the optimisation of techniques such as quantitative ultrasound imaging and targeted drug delivery. Existing characterisation techniques, such as ultra-high speed microscopy provide important insights, but suffer from a number of limitations; most significantly difficulty in obtaining large data sets suitable for statistical analysis and the need to physically constrain the particles, thereby altering their dynamics. Here a microfluidic system is presented that overcomes these challenges to enable the measurement of single echogenic particle response to ultrasound excitation. A co-axial flow focusing device is used to direct a continuous stream of unconstrained particles through the combined focal region of an ultrasound transducer and a laser. Both the optical and acoustic scatter from individual particles are then simultaneously recorded. Calibration of the device and example results for different types of echogenic particle are presented, demonstrating a high throughput of up to 20 particles per second and the ability to resolve changes in particle radius down to 0.1 μm with an uncertainty of less than 3%.

1. Introduction

Echogenic particles offer a wide range of promising applications in biomedical ultrasound for both therapy and diagnosis. There are three main classes of particle currently under research: gas filled microbubbles, volatile liquid micro/nano droplets and sonosensitive solid nanoparticles. The most well known are gas microbubbles with diameters between 1 and 10 μm and stabilised by a surfactant or polymer shell. Bubbles of this size undergo resonant oscillations at clinically relevant ultrasound frequencies[1] giving rise to highly nonlinear scattering that can be exploited for image contrast enhancement, providing a low cost and minimally-invasive tool for vascular imaging.[2] At lower frequencies and/or higher acoustic pressures these oscillations can also produce mechanical and thermal effects that can enhance drug delivery and tissue ablation.[3,4] The microbubble coating enables circulation times of up to several minutes within the bloodstream[5] and the ability to engineer desirable properties such as shell stiffness and viscosity[6] which also affect the bubble's response to ultrasound excitation.[7,8]

Less well established, although increasingly under investigation are droplets of volatile liquids, typically stabilised perfluorocarbon emulsions, that can be vaporised by exposure to ultrasound.[9] The resulting vapour and/or gas bubble can be large enough for the localised occlusion of blood vessels, *e.g.*, to reduce blood flow to a tumour.[9,10] In addition, unlike microbubbles, liquid droplets can be made sufficiently small to pass through the "leaky" endothelial walls that characterise the vasculature of cancerous tissue and act as cavitation nuclei for the enhancement of High Intensity Focused Ultrasound (HIFU) therapies.[3] Solid nanoparticles entrapping gas on their surfaces offer similar advantages, but are more stable and there is evidence that they may provide more sustained cavitation activity.[11]

Unfortunately the highly nonlinear character of the response of echogenic particles to ultrasound and the sensitivity of that response to their physical characteristics makes predicting their behaviour extremely challenging. This has hindered the development of several clinical applications, *e.g.*, quantitative ultrasound imaging for which the relationship between exposure parameters and particle response must be fully characterised.[12] The same is true for therapeutic applications in which the concentration of particles in a target region needs to be quantified. Previous research has focused on either the bulk acoustic properties of microbubble suspensions[13–16] or the characterisation of single microbubbles using both acoustic measurements and direct

Institute of Biomedical Engineering, University of Oxford, Old Road Campus Research Building, Oxford OX3 7DQ, UK. E-mail: eleanor.stride@eng.ox.ac.uk; Tel: +44 (0)1865617747

† Electronic supplementary information (ESI) available. See DOI: 10.1039/c4lc01206b

optical observation. The latter approach is usually preferable as individual bubbles can differ significantly in their response[17] and, as described below, several important phenomena have been identified as a result of such studies using acoustic and/or laser scattering or ultra-high speed imaging.[18–21]

Each of the techniques reported in the literature, however, suffer from one or more of the following limitations: (i) large experimental uncertainties, (ii) the need to physically constrain particle leading to a change in acoustic response and (iii) small data sets unsuitable for statistical analysis. In the present study a microfluidic system is presented that addresses these limitations enabling high throughput characterisation of the unconstrained response of echogenic particles to ultrasound excitation. The following sections describe the underlying principles of the system, its design, construction and calibration and finally measurements obtained with different types of echogenic particle.

1.1 Particle isolation

A key aspect of characterising the acoustic response of single particles is achieving sufficient isolation, *i.e.* observing a particle's response in the absence of physical boundaries and neighbouring particles that may alter its behaviour. Commonly, isolation from other particles is achieved by pumping a highly diluted solution of particles through an optically and acoustically transparent cellulose tube (typically 100–200 μm internal diameter).[22,23] The tube aids in the alignment of optical and acoustic instruments, however the tube wall has been shown to affect the behaviour of microbubbles.[24,25]

In order to eliminate physical interactions with boundaries several different methods have been successfully employed. Acoustic standing waves can be used to manipulate particles by attracting them to the nodes of a standing wave, however particles tend to form clusters and high throughput may not be feasible with this type of system.[26] Acoustic radiation forces could be generated in a flow configuration using much higher ultrasound frequencies to push particles away from a surface; however, this would increase uncertainty in the characterization of the sound field and potentially result in heating of the surrounding liquid, particularly at the higher driving voltages required for high throughput. Techniques based on electrical fields such as dielectrophoresis (DEP) could potentially affect the structure of the lipid coating[27] and require costly and complex equipment.[28] Optical tweezers can be used to counter a microbubble's buoyancy and force it away from the top surface of a capillary tube; this has been utilised in several high speed camera studies.[29] However, a tube is still needed and the time required to isolate a single microbubble makes large sample analysis unfeasible.[30] Hydrodynamic focusing[19,31] is less restrictive in this sense. The method was pioneered for ultrasonic particle analysis in the late 80's by Roos[32] and further developed by Apfel.[33] A hydrodynamically focused flow is produced by two concentric needles each with independently controllable flow rates. The outer flow (sheath flow) causes the inner flow (particle flow) to taper along a well-defined path from the exit of the needles. This approach allows for a very high throughput of particles and control of their spatial location.[33]

With the advent of microfluidic technologies, a range of devices have been developed to achieve two- or three-dimensional hydrodynamic focusing of micro-scale objects.[34] Three-dimensional hydrodynamic focusing can be achieved by different means, *e.g.* by using co-axially aligned microchannels;[35] by exploiting the inertial forces resulting from particle confinement at Reynolds numbers >1 (also known as inertial focusing);[36] by combining inertial focusing with lateral particle drift generated by secondary flows in curved microchannels;[37] by designing for specific microstructures (*e.g.* chevrons) which deflect a particle's trajectory towards a desired location.[38] The main features of co-axial focusing architectures which make them suitable for our application include (i) the need for controlling two inlet flow lines only, (ii) the physical separation between the focused stream and the inner surfaces of the device, (iii) the ease of priming, cleaning and operation.

1.2 Particle characterisation and sizing techniques

As regards the response of echogenic particles to ultrasound, the most significant insights to date have come from ultra high speed imaging studies, including, in the case of microbubbles: non-spherical behaviour,[39] compression-only behaviour,[20] subharmonic thresholds and lipid shedding.[40] Unfortunately, high speed imaging at MHz frequencies is limited by the need for highly specialised equipment, optical diffraction and the complexity of the experiments leading to relatively small sample numbers. Ultrasonic scattering measurements are easier to perform and provide data that are directly relevant to imaging applications. However, acoustic particle sizing is relatively imprecise[41] and there is a trade-off between transducer sensitivity and bandwidth that will inevitably result in a lower signal to noise ratio (SNR) compared to optical measurements.

Light scattering offers many advantages over both high speed imaging and ultrasound scattering measurements. The theory of plane wave light scattering from spherical particles is well established, and has been successfully employed in the sizing of microbubbles[42] and for observing sonoluminescence.[43] Previous work by Matula *et al.*[44,45] has demonstrated the potential of light scattering as a powerful microbubble characterisation technique by adapting a flow cytometry device to include a piezoelectric transducer. High signal to noise ratio (SNR) was achieved, but since in this case the particles must be focused within the flow cell a physical constraint exists that will affect both a particle's response and the acoustic field due to reflections and standing waves. As described below, our design removes this physical boundary, so that the particles are unconstrained and both the incident and scattered acoustic fields can be accurately measured.

2. Theory

The following section provides a brief overview of the theories describing the interaction of a gas cavity with light and ultrasound.

2.1 Sizing of microscale gas cavities

Mie theory describes the scatter of plane wave light from dielectric spherical particles of radius, r. Freely available software, MiePlot by Phillip Laven,[46] was used in this study for simulations. A brief overview is given here, a more detailed explanation may be found by Kerker.[47] The scattered light intensity, I_{Scat} (W/m^2), at the angle θ is equal to a fraction of the initial intensity, I_0, multiplied by the differential scattering cross section, σ'_{Scat}, of the particle.

$$I_{\mathrm{Scat}}(\theta) = I_0 \frac{1}{R^2}\sigma'_{\mathrm{Scat}}(\lambda, r, \theta) \quad (1)$$

The scattered light intensity thus reduces exponentially with distance from the detector, R. The rate of energy scattered over a defined angle range, $\Delta\phi$, can then be calculated as:

$$\dot{E}_{\mathrm{Scat}} = I_0 \frac{\Delta\phi}{R^2}\sigma'_{\mathrm{Scat}} \quad (2)$$

For the sizing of microscale particles a monotonic curve can be obtained by increasing the light collection angle, or aperture (Fig. 1). The effect of a particle's coating, for example on a stabilised microbubble, is much more difficult to predict; previous work by Marston[48] has indicated that the coating effect is negligible since the coating thickness (10–20 nm) is much smaller than the light wavelength.

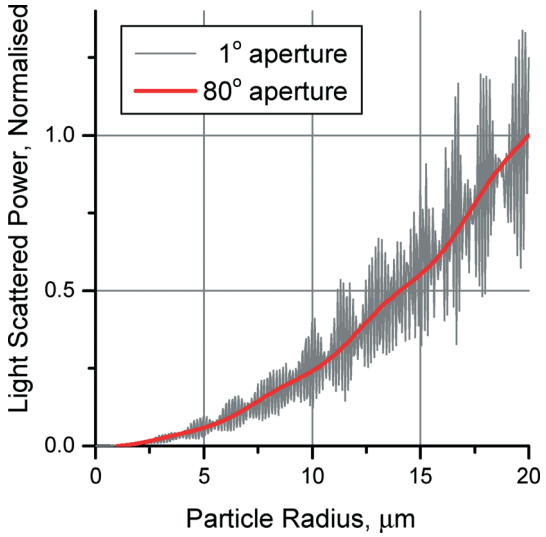

Fig. 1 Mie scattering simulations of the scattered light power (normalised to the scatter from a 20 μm bubble) *vs.* micro-cavity radius (in μm) and light collection aperture. Increasing the aperture provides a monotonic relationship suitable for experimentally estimating a micro-cavity's radius.

The sizing of nanoparticles, *i.e.* particles much smaller than the optical wavelength, using light scattering is also feasible,[49] but due to the sixth power dependency on the particle size it is limited to higher power optical equipment and is not possible with the system described in this study. However, the gas/vapour bubble produced by a nanoparticle can be measured provided it is on the micrometre scale.

2.2 Dynamics of an echogenic particle

As above, echogenic particles may contain a gas core, bubble nucleation site or liquid droplet that undergoes a phase transition to a gaseous state. The resulting volume of gas makes them acoustically responsive. A model for an uncoated bubble undergoing spherical oscillations was first developed by Lord Rayleigh and further developed by various contributors to become the Rayleigh Plesset Noltingk Neppiras Poritsky (RPNNP) equation:[50]

$$\frac{P_{\mathrm{B}}(t) - P_{\infty}(t)}{\rho_{\mathrm{L}}} = r\ddot{r} + \frac{3}{2}\dot{r}^2 + \frac{4\nu_{\mathrm{L}}\dot{r}}{R} + \frac{2s}{\rho_{\mathrm{L}} r} \quad (3)$$

Here the dot notation represents the time derivative, $P_{\mathrm{B}}(t)$ is the time varying pressure within the bubble, $P_{\infty}(t)$ is the external pressure field, ρ_{L} and ν_{L} are the surrounding liquid density and kinematic viscosity, respectively; r is the bubble radius and S is the surface tension. This model has been further developed to incorporate microbubble shell properties, buckling phenomena, and vaporisation and cavitation processes.[51] However, the validation of these models is an ongoing challenge due to the difficulty in determining accurate values for the additional parameters.

3. Materials and methods

3.1 Co-axial microfluidic device for particle isolation

Central to the system is the isolation of particles away from physical boundaries within the confocal area of the optical and acoustic instruments. In our design this is achieved using a hydrodynamically focused flow. To enable this, a custom microfluidic co-axial focusing device was designed (Fig. 2). An all glass device (fabricated by GPE Scientific) was selected to ensure concentricity of the needles, ease of cleaning and because it would allow for visualisation of the flow and detection of unwanted gas pockets.

For the operation of the microfluidic device, echogenic particles are diluted to a concentration on the order of 10^5 particles ml^{-1} with filtered (0.2 μm) de-ionised water and placed in a syringe connected to the particle flow channel of the microfluidic device. Both the particle and sheath (filtered deionised water, degassed for sheath flow) flows are driven by syringe pumps (World Precision Instruments, model AL-1000, Sarasota, Florida).

Due to the nature of echogenic particles, care must be taken during handling and loading into the microfluidic device. Air traps should be added to the syringes to reduce flow pulsations and pressure waves that may arise from

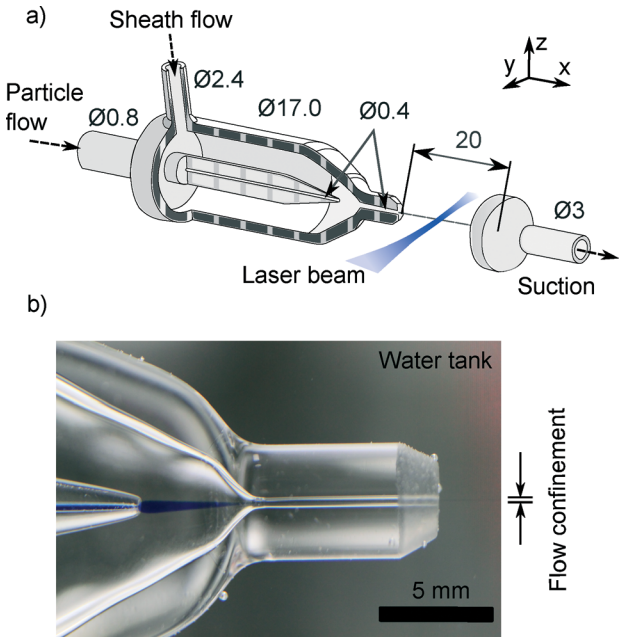

Fig. 2 A microfluidic hydrodynamic focusing device for the isolation of echogenic particles in free space: a) design of device with a suction element 20 mm away from the nozzle exit. All dimensions are given in mm and material is glass, surfaces are grounded and polished. b) Photograph of device to demonstrate focusing of particle flow (blue ink). Glass enables flow visualisation and checking for unwanted gas pockets that may otherwise disturb the flow.

changing of flow rates or connecting tubing. The back pressure, ΔP, generated from a liquid with a kinematic viscosity, v, and flow rate, Q, in tubing of length L is inversely proportional to the fourth power of tubing diameter d:

$$\Delta P \propto \left(\frac{QLv}{d^4}\right) \quad (4)$$

For the setup presented in this paper, not considering tubing connections, the maximum generated back pressure is of the order of a few Pascals. This is insignificant when compared to clinical ultrasound pressures and the physiological variation in human blood pressure of up to 120 mmHg (~16 kPa).[52]

3.2 Experimental set up

A schematic of the system is shown in Fig. 3. The key components are the co-axial microfluidic flow focusing device, ultrasound transducer(s), laser and optical detector. The system is submerged in a water tank to enable efficient acoustic coupling and temperature control. Manual positioning stages (model 443, Newport), secured to an external frame, allow precise alignment of the laser, microscope objective, microfluidic device and ultrasound transducer. The system has been designed to enable substitution of different ultrasonic and optical components, *e.g.* to vary the frequency of ultrasound excitation.

Measurements are performed as follows: (i) particles are isolated and streamed into the focal zone of the laser, microscope objective and ultrasound transducer, (ii) as a particle passes through the laser beam, light is scattered and detected by a photomultiplier tube (PMT), (iii) this triggers ultrasound excitation while the particle is still in the laser beam and the resulting particle response can be recorded from the scattered light and acoustic pressure.

To maximise the SNR, defined as the smallest change in gas cavity radius detectable over the RMS of background signal, the following optical components were used: (i) a 4.5 mW laser diode (405 nm, Thorlabs) focused using a single plano-convex lens (f = 30 mm, #69-339, Edmund Optics) built into a water tight casing, (ii) a 0.8 Numerical Aperture (NA) water immersible microscope objective (3 mm working distance, LUMPLFLN 40XW Olympus) and (iii) a 405 nm laser line filter (FB405-10, Thorlabs) and a custom built light beam dump to stop light from reflecting within the tank. For the detection of scattered light a PMT with an inbuilt DC – 8 MHz

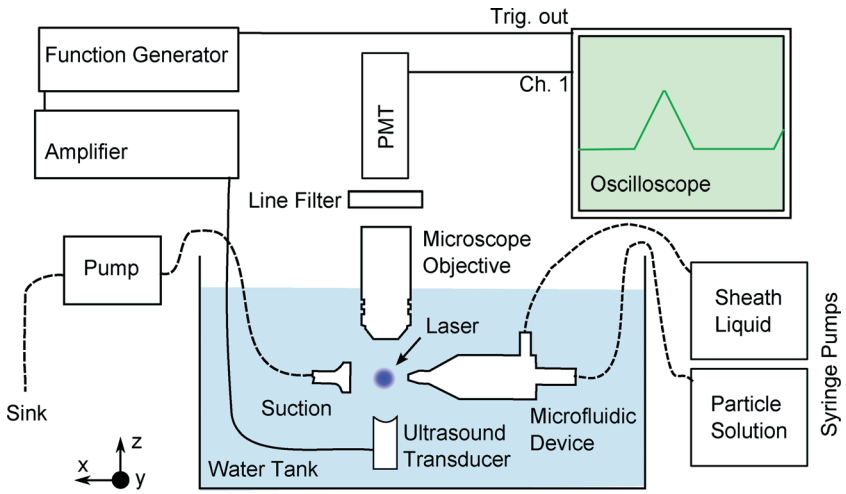

Fig. 3 Schematic diagram (not to scale) for the characterisation of single echogenic particles using light scattering. The coaxial device and suction element are shown in greater detail in Fig. 2. Dotted lines indicate fluid flows.

low pass amplifier (H10493-003, Hamamatsu) was employed. PMTs provide a higher sensitivity in low light conditions with lower dark and gain noise than avalanche diodes, although care must be taken not to exceed the saturation limit above which point the relationship between light intensity and voltage is no longer linear.

Alignment of the laser, microscope objective and particle stream was achieved by maximising the PMT output on an oscilloscope (Waverunner 64Xi, Lecroy); scattering of the laser beam from impurities in the water allows the focal plane of the microscope objective to be aligned with that of the laser, from which the maximum scattered light signal will be detected by the PMT. To align the particle stream, size standard polystyrene microspheres were added to the particle flow of the microfluidic device (see below) and the light scattering amplitude maximised by adjusting its position.

It is important to ensure that all particles experience a similar acoustic pressure field during ultrasound excitation to enable comparison of their responses. For low acoustic pressures (kPa) unfocused ultrasound transducers may be used which, at the scale of a single microbubble, can be assumed to produce a uniform acoustic field. For higher pressures (MPa), however, focused transducers are required and so the acoustic field will vary with a Gaussian or similar profile. The effective width of the beam is directly proportional to the frequency of excitation and must be significantly larger than any variation in particle location in the focused flow. Provided this condition is met, however, the system offers considerable advantages over other techniques in which particle location and hence excitation pressure may be poorly defined.[19] Here, because the laser is used to trigger the ultrasound excitation, the location of the particle with respect to the optical and ultrasound foci is also always known.

Particles travelling through the laser beam are detected using a gradient threshold. The dynamic range and threshold value on the oscilloscope can be manually adjusted during an experiment to capture differently sized particles. Once a particle is detected, the oscilloscope sends a trigger signal to the function generator (Agilent, model 33220A, Berkshire, UK) which in turn sends the desired driving wave form, amplified by 50 dB (Electric and Innovation, model 325LA, Rochester, NY), to the ultrasound transducer. Since the speed of sound is significantly smaller than the speed of light, the acoustic sound wave will only reach the particle 10–30 μs later (Fig. 4), depending on the transducer focal length. For calibration of the acoustic field a fibre-optic hydrophone (90 degree acceptance, Precision Acoustics, Dorset) can replace the microscope objective, and the acoustic field experienced by the particles is measured by moving the tip of the fibre into the focus of the laser beam.

A further inherent advantage of this system is the ease with which unwanted particles, such as dust motes introduced from the water tank, can be excluded from analysis based on the time taken to pass through the laser beam. Since the flow velocity profile will be approximately parabolic, the time of travel will be correlated to the particle position in the flow. Particles of interest will be travelling the fastest at the centre of the flow and take the least time to travel through the laser beam.

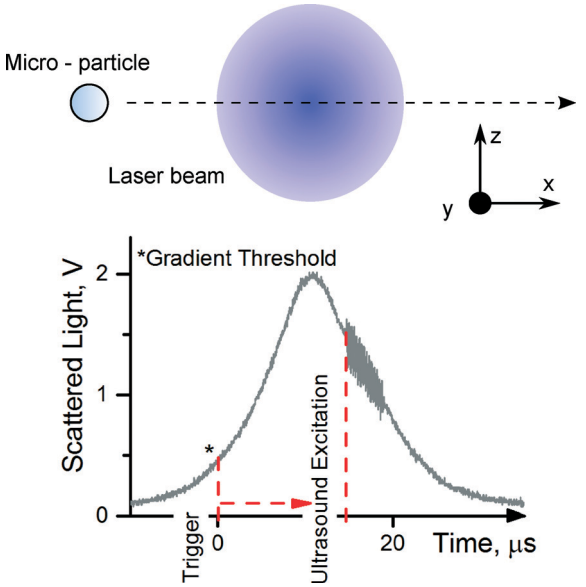

Fig. 4 Demonstration of particle detection and ultrasound excitation. Ultrasound excitation is triggered from a gradient threshold (in the scattered light signal) as the particle enters the laser beam. After a short delay the ultrasound wave reaches the particle while it is still traversing the laser beam and the resulting volume oscillation is recorded. Data shown are for a SonoVue® microbubble.

3.3 Computational fluid dynamic simulations

A three-dimensional (3D) numerical model was developed as a design tool to predict and characterise the fluid dynamic field and the trajectories of particles exiting the microfluidic device. This proved to be particularly useful to verify if the particles' flow behaviour (*i.e.*, position in the focused stream and velocity) was compatible with the system's requirements for particle detection/excitation, under a range of different operational conditions (*i.e.*, inlet flow rates and particle's physical properties). The model geometry was constructed and meshed using ICEM CFD 14.5 (Ansys Inc., USA). The geometry consisted of two components, (i) the co-axial flow focusing device and (ii) the suction element. A truncated cone was designed to join the two components, so as to model the outer fluid surrounding the focused stream within the water tank (Fig. S1a†).

The geometry was meshed using tetrahedral elements (total number of elements = 4 914 892). A boundary-layer meshing strategy was adopted, with mesh element size reducing from the outer surfaces towards the focused fluid stream. The transition in mesh element size was controlled by generating interior surfaces coaxially with the focused stream (Fig. S1b†). The equations for mass conservation (eqn (5)) and momentum conservation (eqn (6)) were solved over the computational flow domain, using Ansys Fluent (version 14.5, Ansys Inc., USA):

$$\nabla\cdot(v) = 0 \quad (5)$$

$$\rho\frac{\partial v}{\partial t} + \rho v\nabla v = -\nabla P + \mu\nabla^2 v \quad (6)$$

where v, ρ, μ and P are fluid velocity, density, dynamic viscosity and pressure, respectively. The working fluid was assumed to be incompressible and Newtonian, with a density of 1000 kg m^{-3} and a dynamic viscosity of 0.001 Pa s. The flow was assumed to be steady and laminar. The Semi-Implicit Method for Pressure-Linked Equations (SIMPLE) algorithm was employed for solving the governing equations. A second-order upwind discretization scheme was adopted to discretize the momentum equations, and a second-order scheme was adopted for pressure interpolation. Mass flow boundary conditions were applied at the inlets of the microfluidic device (Fig. S1b†). An outflow boundary condition was applied at the suction element (flow rate weighting = 1). In order to reproduce the effect of fluid suctioning generated by the vacuum pump, a mass flow inlet boundary condition was applied at the surface of the truncated cone joining the microfluidic device with the suction element (Fig. S1b†). This flow rate was set equal to the difference between the total flow entering the microfluidic device and the flow exiting the suction element (which was experimentally defined). Walls were assumed to be rigid, with a no slip flow boundary condition.

A simplified, one-way discrete phase model was adopted to predict the microbubbles' flow behaviour. The model included the contribution of Saffman lift force. A suspension of microbubbles was injected from the central inlet of the microfluidic device. The microbubbles' diameter followed a Rosin-Rammler distribution,[53] with minimum diameter = 1 μm, maximum diameter = 15 μm, mean diameter = 3.5 μm, and spread parameter = 0.8. A custom built MATLAB (R2012a, The Math Works Inc.) script was used to process the numerical data and determine the radial position and velocity of microbubbles exiting the microfluidic device.

3.4 Calibration

3.4.1 Flow and particle confinement. Calibrations were performed to investigate the effect of sheath and particle flow rates on the downstream particle confinement. Standard pen ink was added to the particle flow solution and the resulting ink flow diameter 6 mm downstream from the exit of the microfluidic device was measured optically. Images were captured by replacing the PMT with a USB camera (DCU224M, Thorlabs) in line with the 40× microscope objective (Fig. 3). Since a particle's trajectory may differ from the fluid path lines due to differences in densities and the effect of lift forces, SonoVue® (Bracco Diagnostics) microbubbles were then added to the particle flow and their trajectories filmed at 50 000 frames per second (fps) using a high speed camera (Memrecam HX-4, NAC), in place of the USB camera. For both experiments the images were processed offline using ImageJ (NIH, USA) to measure the focused flow diameter (see Fig. S3†) and the MosaicSuite (ImageJ) for particle tracking using the high speed imaging.

3.4.2 Sizing sensitivity. To assess the sensitivity and accuracy of the optical set up, samples of three different size standard polystyrene microspheres (Polysciences, Int.) with mean diameters of 0.9, 4.52 and 11 μm, were diluted and added separately to the particle flow. To prevent inter-particle clustering, 0.1 ml of Tween 20 was added to the microsphere solutions (3 ml). Sheath and particle flow rates were set to 5 ml min^{-1} and 30 μl min^{-1} respectively for all runs. The dynamic range of the oscilloscope was set for each different size such that the light scattering intensity was at least three quarters of the available range. As described previously, scattering events were recorded on the oscilloscope once a manually set gradient threshold was reached. Data were then transferred to a PC and the maximum voltage of each trace measured using a custom written MATLAB (R2012a, The Math Works Inc.) script. Mie scattering simulations were performed for comparison to experimental results, using refractive indices of 1 and 1.6 for water and polystyrene respectively, laser wavelength of 405 nm and an aperture of 80° perpendicular to the laser beam (corresponding to the 0.8 NA of the objective used).

3.5 Particle measurements

To demonstrate the apparatus' potential for characterising microbubbles and other echogenic particles, experiments were performed using both gas microbubbles and volatile liquid droplets. Freshly prepared SonoVue® microbubbles were diluted 1 : 60 with 0.2 μm filtered deionised water for the particle flow. An unfocused 3.5 MHz ultrasound transducer (Panametrics-NDT, Waltham, MA) was used to excite each microbubble with 10 cycles, while the peak negative pressure was varied from 9 to 14 kPa.

Volatile perfluoropentane (PFP) droplets, prepared in house as described in section S2,† were passed through the particle flow. Due to their size (200 nm to 600 nm with a mean of 350 nm, measured using dynamic light scattering) detection of individual particles was not possible. However, at least a reasonable proportion of the particles produced sufficient optical scattering to trigger ultrasound excitation and the resulting gas cavities were easily detectable and could be sized as described above. A 1 MHz centre frequency transducer (Panametrics-NDT, Waltham, MA) was used with acoustic field parameters of 25 cycle of 1 MHz at 1 MPa peak negative pressure.

All scattering events were recorded at a sampling rate of 25 MHz and transferred to a hard drive. Scattering events were recorded at approximately 10–20 per second, depending on the particles dilution and flow rates, and analysed offline on a custom written MATLAB (R2012a, The Math Works Inc.) program.

3.6 Uncertainty

3.6.1 ADC quantisation. Quantisation of the analogue light intensity signal from the PMT will introduce an error

proportional to the 8-bit oscilloscope's (256 levels) dynamic range. This presents an inconvenience for the detection of oscillations that are significantly smaller than the size of the gas cavity. The theoretical uncertainty, assuming a dynamic range such that light scatter due to the gas cavity size fills 50% of the available range gives an error of 0.78% of particle radius.

3.6.2 Spatial sensitivity. Spatial sensitivity refers to the error generated due to variation in a particle's location in the laser beam. Given a variation of z μm and assuming that the laser intensity is a Gaussian distribution, where ω_0 is the Gaussian beam radius. The variation in laser intensity, I, can be estimated as:

$$\Delta I = 1 - \exp\left[-\frac{2z^2}{\omega_0{}^2}\right] \quad (7)$$

The uncertainty in laser intensity, for estimating the gas cavity size, can be reduced therefore by increasing the laser's beam width to reduce the effect of a particle's spatial variation. A larger beam also provides more time to interrogate a particle as it travels through, however the maximum intensity and hence the SNR will be reduced.

4. Results and discussion

4.1 Hydrodynamically focused flow confinement

The confinement of ink downstream of the co-axial microfluidic device was assessed to optimise the sheath and particle flow rates. The focused flow was observed to be stable in the open water tank between the microfluidic device and suction element approximately 20 mm away.

Ink was first added to the particle flow and the downstream flow confinement (see Fig. 2b) was measured for particle flow rates of 10 to 60 μl min^{-1} and sheath flow rates of 3 to 9 ml min^{-1}, Fig. 5. The smallest confinement in the y axis (optical imaging limited to 2D) of the ink was 12 μm (particle and sheath flow rates of 10 μl min^{-1} and 9 ml min^{-1} respectively) with control up to 57 μm. Fluid streamlines were also determined computationally, and good agreement with the experimental results was observed (Fig. 5), validating the use of the computational model to investigate the confinement of particles.

4.2 Hydrodynamically focused particle confinement

High speed imaging was used to observe a variation in particle position in the y axis of 33.3 μm using SonoVue® microbubbles 6 mm downstream from the microfluidic device (particle and sheath flow rates of 20 μl min^{-1} and 3 ml min^{-1} respectively). Fig. 6d shows the superimposed paths of individual bubbles from multiple runs. Diluted polystyrene microparticles were also observed at the exit of the device to verify that the particles were isolated from each other, see video S1.† Numerical simulations were then performed (examples of the simulated flow fields are shown in Fig. S4†) to predict particle trajectories and velocities under a wider range of experimental conditions, providing a useful tool to fully characterise the system's performance. Simulations of the particle's confinement (Fig. 6c) agreed well with the high speed observation and demonstrate that the particles' flow is more confined in the z axis (Fig. 6a) which was not possible to image experimentally. The z axis confinement is more important for assessing the sensitivity to variation in a particle's location; in the y axis the laser beam intensity varies with the focusing of the laser beam, this is however far more gradual than the variation due to the Gaussian beam as seen in the z axis (refer to Fig. 4). Computational simulations show that the mean particle velocity varies linearly with sheath flow rate (from 0.23 to 0.68 m s^{-1} at sheath flow rates of 3 and 7 ml min^{-1}) and it is not significantly affected by the particle flow rate. Particle velocity determines the time through the laser beam and can therefore be used to estimate the laser beam diameter at the intersection with the particle's trajectory (Fig. 4).

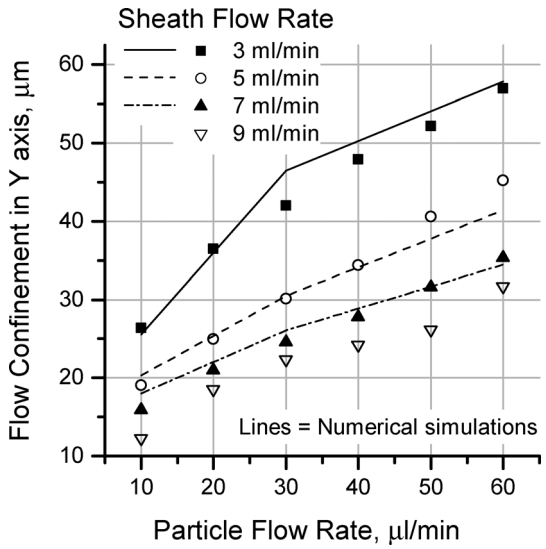

Fig. 5 Effect of sheath and particle flow rates on the hydrodynamic flow confinement 6 mm downstream from the exit of the microfluidic device. Numerical simulations (lines) are shown together with the experimental points (symbols). Please see also Fig. S3.†

Notably, numerical results show that under a range of different operational conditions and particles' dimensions, (i) particle's confinement can be restricted down to 10 μm for accurate sizing within the laser beam, (ii) particle's velocity enables ultrasound excitation while the particle is still traversing the laser beam, and (iii) it is possible to adjust the particles' confinement by finely controlling the flow rate ratio between the two inlet lines, at high-throughput total flow rates.

4.3 Sizing calibration

Measurements from size standard microparticles were compared with Mie scattering simulations to assess the sizing sensitivity and accuracy of the apparatus (Fig. 7). Light scattering from the microparticles was found to agree well with Mie theory predictions and the standard deviation in light

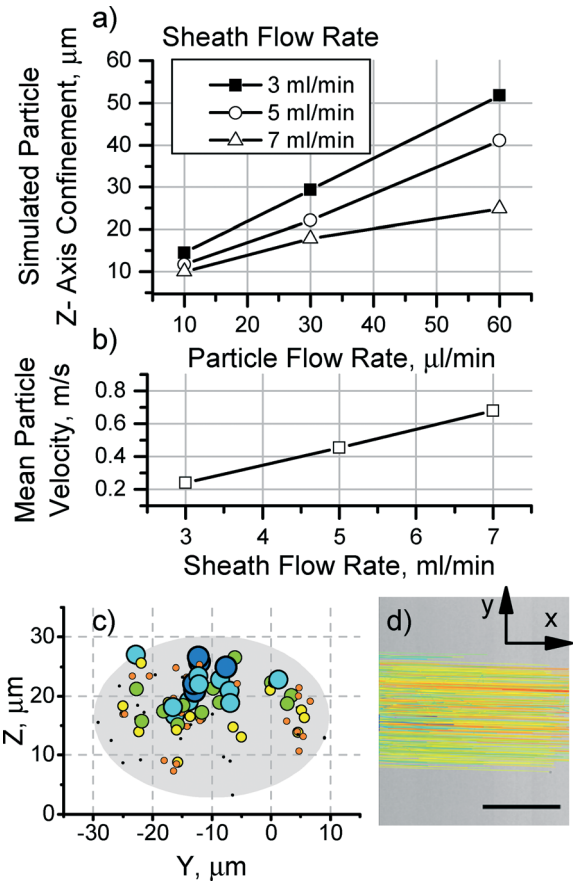

Fig. 6 Simulations from particle tracking (density 1.331 kg m^{-3}, radii between 1 to 15 µm with a mean radius of 3.5 µm). a) Confinement of particles along the *z* axis, where confinement is the largest distance between two particles. b) Particle velocities as a function of outer flow rate. c) Example of particle spatial spread (n = 93) downstream, 6 mm away from the nozzle exit, particle radius is represented by the marker size, larger microbubbles tend towards the top of the distribution due to the likely combined effect of buoyancy and lift forces. Outer flow rate = 3 ml min^{-1}, inner flow rate = 20 µl min^{-1}. d) Experimental data of SonoVue® microbubbles at same flow conditions at c, recorded using a high speed camera at 50 kfps, each line represents the path of a single bubble which could be compared with the simulated trajectories. Scale bar = 20 µm.

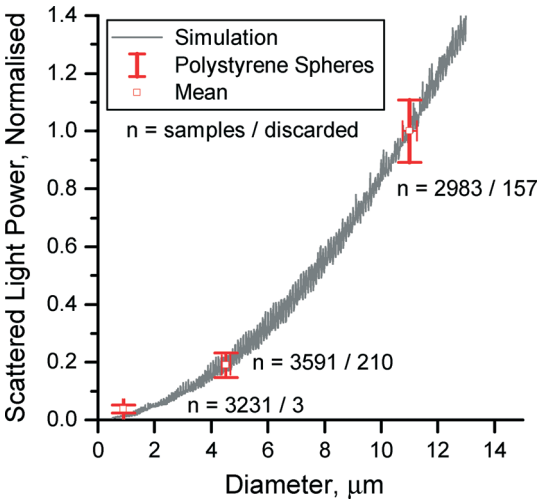

Fig. 7 Sizing and sensitivity calibration using size standard polystyrene microparticles. Light scattering results (vertical red bars represent ± standard deviation in light scattering intensity, horizontal red bars represent standard deviation in microparticles size from manufacture's specification) are compared to Mie scattering simulations of the polystyrene microparticles (refractive indices of water = 1 and microparticles = 1.6, unpolarised light at 405 nm, 80° aperture). Discarded samples refer to particles outside of the normal transit time through the laser beam. The scattered light intensity is normalised with respect to the Mie scattering estimation for an 11 µm microsphere.

scattering (vertical bars) was also in agreement with the standard deviation in microparticle size (horizontal bars). This provided the means of calibrating the system for sizing of gas cavities.

4.4 Applications

A few examples are given to demonstrate the potential applications of the new apparatus.

4.4.1 SonoVue® radius–time curves. At the simulated particle velocities (0.46 m s^{-1} for an sheath flow rate of 5 ml min^{-1}, Fig. 6) a throughput on the order of thousands of particles per second is feasible, however due to the speed of writing data to the oscilloscope's hard drive and high dilution of particles the throughput is much lower. For the data presented below a throughput of approximately 20 particles per second allowed the collection of over 12 000 individual SonoVue® microbubbles over the course of 30 minutes; 4 example traces are shown in Fig. 8 to demonstrate the range of radii captured. Two of the microbubbles display 'compression-only' behaviour, *i.e.* the bubble exhibits unsymmetrical oscillations, with negligible expansion during the rarefaction phase of each ultrasound cycle. This is due to saturation of the phospholipid coating.[20] Another bubble shows a significant sub-harmonic response, which is desirable for contrast enhanced ultrasound imaging. From the data obtained the size distribution can also be determined simultaneously (Fig. 8c). This is not otherwise known and can be time consuming to measure using normal microscopy or other particle sizing techniques.[54] In addition, the mean frequency responses were calculated to demonstrate the use of processing a large number of samples, Fig. 9.

4.4.2 Observing the vaporisation of volatile droplets. Fig. 10 shows the trace of a perfluoropentane (PFP) droplet following vaporisation. A highly non-linear response is observed with multiple harmonics and fractional harmonics. This indicates that the apparatus provides a powerful method for assessing the cavitation thresholds and subsequent behaviour of volatile droplets and cavitation nuclei.

4.4.3 Uncertainty analysis. Variation in a particle's confinement along the *z* axis will lead to uncertainty in the laser intensity and subsequently the estimated micro-cavity radius. Using Mie theory the uncertainty has been estimated for varying laser beam width and particle confinement, Fig. 11. The −6 dB width of the laser beam used in this apparatus was measured to be 250 µm giving an estimated theoretical error of less than 2% of the micro-cavity radius

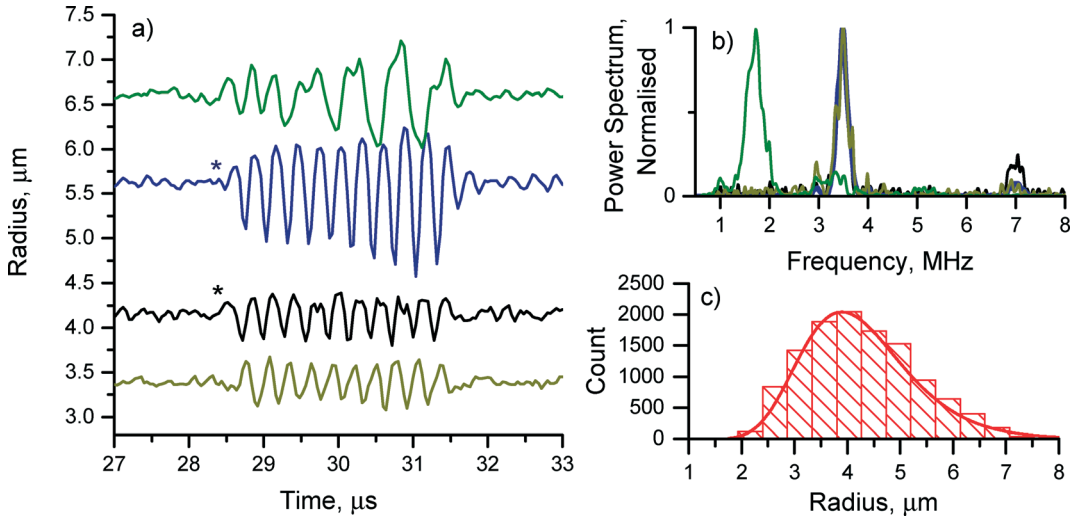

Fig. 8 Examples of a) radius–time curves from SonoVue® microbubbles of different radii, the corresponding b) power spectra and c) the measured size distribution estimated from the light scattering data and Mie theory. Ultrasound parameters: 10 cycles of 3.5 MHz at peak negative pressure of 14 kPa. * indicates compression-only behaviour.

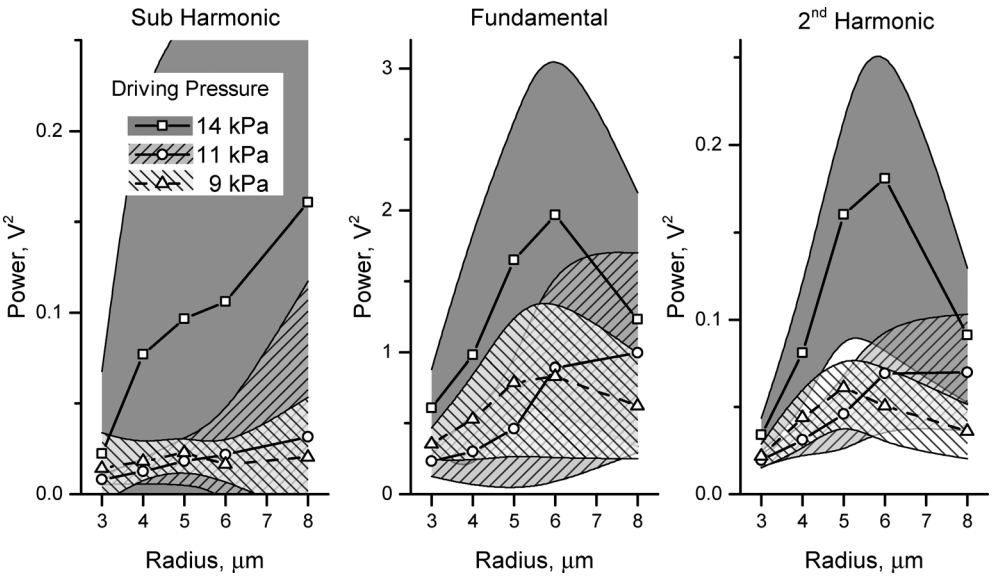

Fig. 9 SonoVue® mean subharmonic, fundamental and 2nd harmonic light scattered power *vs.* radius. Over 12 000 individual SonoVue® microbubbles were analysed. Ultrasound parameters: 10 cycles of 3.5 MHz at varying driving pressures. Samples are divided into radius bins such that there are no less than 100 samples in each bin. Shaded areas represent ±0.5 standard deviation, demonstrating a large variability in acoustic response.

for a flow confinement of 20 μm. A further uncertainty of 0.78% is introduced due to the ADC quantisation, as mentioned previously, giving an overall estimated error of less than 3%. The noise floor, given as the maximum RMS noise measured from the SonoVue® samples, was approximately 100 nm when converted to radius using Mie scattering theory.

As mentioned previously, the focused laser beam allows for accurate positioning of the hydrophone to measure the acoustic field at the interrogation site. The error in acoustic calibration is therefore assumed to be negligible given the acoustic beam width is significantly larger than the laser beam width.

5. Limitations and future work

Light scattering as applied in this study is limited in that it only provides a one dimensional representation of the particle. In converting the optical scattering measurements into radial oscillations it is implicitly assumed that the gas cavity remains spherical. Previous high speed video microscopy studies have however demonstrated that ultrasound contrast agent microbubbles will exhibit non-spherical oscillations even in the absence of a nearby boundary, particularly when driven at frequencies close to their linear resonance frequency.[39] Further investigation is therefore needed as to the

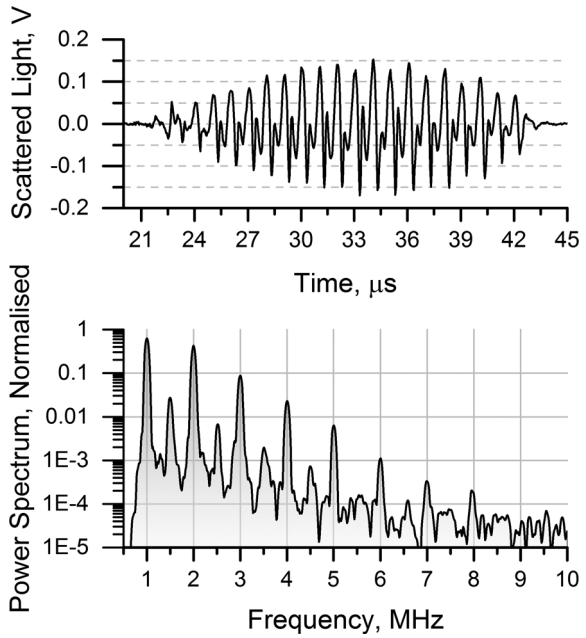

Fig. 10 Example of light scattering due to the vaporisation of a liquid PFP droplet. The power spectrum demonstrates the high bandwidth of the light scattering method. Ultrasound parameters: 25 cycles at 1 MHz at 1 MPa peak negative pressure.

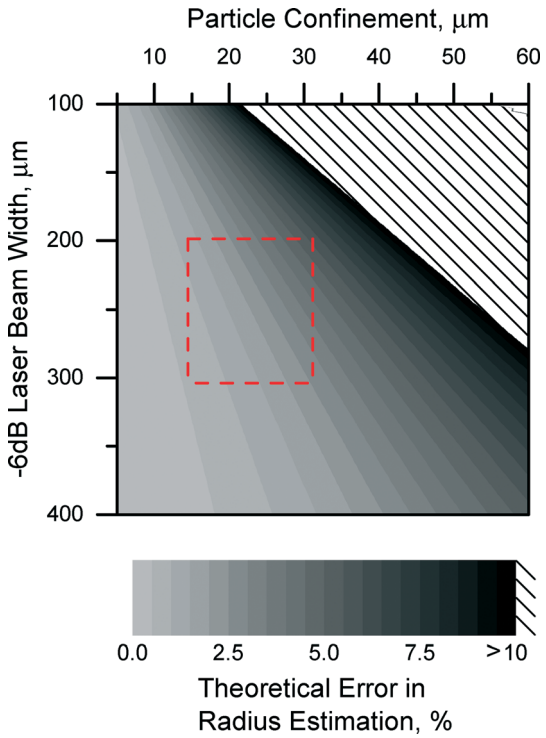

Fig. 11 Theoretical error in particle radius estimation due to the variation in a particle's confinement while travelling through a Gaussian laser beam. Conditions are shown for varying laser beam width and particle confinement; the red dashed box indicates the approximate operating area for the conditions described in this study.

dependence of the optical scatter upon the orientation of a particle passing through the laser beam. This would require either multiple photodetectors or coupling an ultrahigh speed imaging device into the system which was unfortunately outside the scope of the present study. It is hoped that this may be possible in future work however as it could enable the relative contribution of spherical and non-spherical oscillations to the acoustic scattered signal to be determined. This is important for understanding the origin of the nonlinear signal components that are exploited in many contrast enhanced imaging protocols.

The influence of the particle composition and shell thickness has not been adequately assessed to estimate the effect this will have on the Mie Scattering. Numerical simulations have shown that small changes in the real or imaginary refractive index due to the coating may result in significant bias.[55] Despite this, by using a large aperture for light detection the scattering can be assumed to be monotonic, such that the relative particle sizes can be estimated. Regarding the choice of equipment, there is a limited bandwidth obtainable using the PMT's built in amplifier of DC – 8 MHz. Using an amplifier with a higher bandwidth will reduce the SNR but, based on the low noise achieved here, should not significantly affect the accuracy of this method.

6. Conclusion

This study describes the development of a system for measuring the response of single echogenic microparticles to ultrasound excitation with low uncertainty in the measurement of particle size and ultrasound field, isolation of particles from physical boundaries and other microparticles and high throughput for collection of large data set suitable for statistical analysis. Measurements were carried out of the response of both gas microbubbles and liquid nanodroplets at up to 20 particles per second with an estimated uncertainty of less than 3% of the particle radius and with a RMS noise floor corresponding to a resolution of 100 nm. Importantly, the developed system could be employed for high-throughput characterisation of a wider range of different micro-particles (*i.e. via* coupling with particle generation units), which is a widely recognised need in the microfluidic community; particularly to facilitate the industrial translation of newly developed micro- and nano-devices.

Acknowledgements

The authors gratefully acknowledge support from the RCUK Digital Economy Programme (grant number EP/G036861/1 Oxford Centre for Doctoral Training in Healthcare Innovation) and the Engineering and Physical Sciences Research Council (EP/I021795/1). The authors would also like to thank Ronald Roy and Glynn Holt for their technical help, GPE Scientific for their design advice and fabrication of the co-axial microfluidic device and Jim Fisk and Dave Salisbury for fabrication of the rig components.

References

1 E. Stride and N. Saffari, *Proc. Inst. Mech. Eng., Part H*, 2003, **217**, 429–447.
2 J. R. Lindner, *Nat. Rev. Drug Discovery*, 2004, **3**, 527–532.
3 C. C. Coussios and R. A. Roy, *Annu. Rev. Fluid Mech.*, 2008, **40**, 395–420.
4 C. C. Coussios, C. H. Farny, G. Ter Haar and R. A. Roy, *Int. J. Hyperthermia*, 2007, **23**, 105–120.
5 E. Quaia, *Eur. Radiol.*, 2007, **17**, 1995–2008.
6 K. Ferrara, R. Pollard and M. Borden, *Annu. Rev. Biomed. Eng.*, 2007, **9**, 415–447.
7 N. A. Hosny, G. Mohamedi, P. Rademeyer, J. Owen, Y. Wu, M.-X. Tang, R. J. Eckersley, E. Stride and M. K. Kuimova, *Proc. Natl. Acad. Sci. U. S. A.*, 2013, **110**, 9225–9230.
8 S. H. Bloch, R. E. Short, K. W. Ferrara and E. R. Wisner, *Ultrasound Med. Biol.*, 2005, **31**, 439–444.
9 O. D. Kripfgans, J. B. Fowlkes and D. L. Miller, *Ultrasound Med. Biol.*, 2000, **26**, 1177–1189.
10 M.-P. S. Sheeran and P. A. Dayton, *Curr. Pharm. Des.*, 2012, **18**, 2152–2165.
11 S. J. Wagstaffe, H. A. Schiffter, M. Arora and C.-C. Coussios, in *11th International Symposium on Therapeutic Ultrasound, AIP Conf. Proc.*, 2012, pp. 426–431.
12 M.-X. Tang, H. Mulvana, T. Gauthier, A. K. P. Lim, D. O. Cosgrove, R. J. Eckersley and E. Stride, *Interface Focus*, 2011, **1**, 520–539.
13 E. Biagi, L. Breschi, E. Vannacci and L. Masotti, *IEEE Trans. Ultrason. Ferroelectr. Freq. Control*, 2006, **53**, 2174–2182.
14 T. Faez, D. Goertz and N. de Jong, *Ultrasound Med. Biol.*, 2011, **37**, 338–342.
15 P. M. Shankar, P. D. Krishna and V. L. Newhouse, *J. Acoust. Soc. Am.*, 1999, **106**, 2104–2110.
16 D. E. Goertz, N. de Jong and A. F. W. van der Steen, *Ultrasound Med. Biol.*, 2007, **33**, 1376–1388.
17 M. Postema and A. Bouakaz, *IEEE Trans. Ultrason. Ferroelectr. Freq. Control*, 2003, 50.
18 J. Tu, J. Guan, Y. Qiu and T. J. Matula, *J. Acoust. Soc. Am.*, 2009, **126**, 2954–2962.
19 V. Sboros, S. D. Pye, C. A. Macdonald, J. Gomatam, C. M. Moran and W. N. McDicken, *Ultrasound Med. Biol.*, 2005, **31**, 1063–1072.
20 J. Sijl, M. Overvelde, B. Dollet, V. Garbin, N. de Jong, D. Lohse and M. Versluis, *J. Acoust. Soc. Am.*, 2011, **129**, 1729–1739.
21 G. Renaud, J. G. Bosch, A. F. W. Van Der Steen and N. de Jong, *Ultrasound Med. Biol.*, 2014, **40**, 1282–1295.
22 F. Guidi, H. Vos and R. Mori, *IEEE Trans. Ultrason. Ferroelectr. Freq. Control*, 2010, **57**, 193–202.
23 K. E. Morgan, J. S. Allen, P. A. Dayton, J. E. Chomas, L. Klibaov and K. W. Ferrara, *IEEE Trans. Ultrason. Ferroelectr. Freq. Control*, 2000, **47**, 1494–1509.
24 C. F. Caskey, D. E. Kruse, P. A. Dayton, T. K. Kitano and K. W. Ferrara, *Appl. Phys. Lett.*, 2006, **88**, 033902.
25 D. Thomas, V. Sboros, M. Emmer, H. J. Vos and N. de Jong, in *2009 IEEE International Ultrasonics Symposium*, IEEE, 2009, pp. 2782–2784.
26 A. L. Bernassau, P. G. A. Macpherson, J. Beeley, B. W. Drinkwater and D. R. S. Cumming, *Biomed. Microdevices*, 2013, **15**, 289–297.
27 V. Froude and Y. Zhu, *J. Phys. Chem. B*, 2009, **113**, 1552–1558.
28 H. Mulvana, S. Cochran and M. Hill, *Adv. Drug Delivery Rev.*, 2013, **65**, 1600–1610.
29 V. Garbin, D. Cojoc, E. Ferrari, E. Di Fabrizio, M. L. J. Overvelde, S. M. van der Meer, N. de Jong, D. Lohse and M. Versluis, *Appl. Phys. Lett.*, 2007, **90**, 114103.
30 V. Garbin, *Ph.D. Thesis*, University of Trieste, 2006.
31 R. Roy, *Ph.D. Thesis*, Yale University, 1987.
32 M. Roos, *J. Acoust. Soc. Am.*, 1988, **83**, 770–776.
33 R. Roy and R. Apfel, *J. Acoust. Soc. Am.*, 1990, **87**, 2332–2341.
34 X. Xuan, J. Zhu and C. Church, *Microfluid. Nanofluid.*, 2010, **9**, 1–16.
35 P. Paiè, F. Bragheri, R. M. Vazquez and R. Osellame, *Lab Chip*, 2014, **14**, 1826–1833.
36 S. C. Hur, S.-E. Choi, S. Kwon and D. Di Carlo, *Appl. Phys. Lett.*, 2011, **99**, 044101.
37 J. Oakey, R. W. Applegate, E. Arellano, D. Di Carlo, S. W. Graves and M. Toner, *Anal. Chem.*, 2010, **82**, 3862–3867.
38 J. P. Golden, J. S. Kim, J. S. Erickson, L. R. Hilliard, P. B. Howell, G. P. Anderson, M. Nasir and F. S. Ligler, *Lab Chip*, 2009, **9**, 1942–1950.
39 B. Dollet, S. M. van der Meer, V. Garbin, N. de Jong, D. Lohse and M. Versluis, *Ultrasound Med. Biol.*, 2008, **34**, 1465–1473.
40 Y. Luan, G. Lajoinie, E. Gelderblom, I. Skachkov, A. F. W. van der Steen, H. J. Vos, M. Versluis and N. de Jong, *Ultrasound Med. Biol.*, 2014, **40**, 1834–1846.
41 D. Maresca, M. Emmer, P. L. M. J. van Neer, H. J. Vos, M. Versluis, M. Muller, N. de Jong and A. F. W. van der Steen, *Ultrasound Med. Biol.*, 2010, **36**, 1713–1721.
42 S. J. Satinover, J. D. Dove and M. A. Borden, *Ultrasound Med. Biol.*, 2014, **40**, 138–147.
43 D. Gaitan and L. Crum, *J. Acoust. Soc. Am.*, 1992, **91**, 3166–3183.
44 T. J. Matula, J. Swalwell, J. Tu, W. Cui and W. Chen, in *2011 IEEE International Ultrasonics Symposium*, IEEE, 2011, pp. 156–159.
45 J. Guan and T. J. Matula, *J. Acoust. Soc. Am.*, 2004, **116**, 2832.
46 P. Laven, *MiePlot, version 4.3.05*, 2014.
47 M. Kerker, *The scattering of light and other electromagnetic radiation*, Academic Press, New York, 1969.
48 P. L. Marston, S. C. Billette and C. E. Dean, *Proc. SPIE*, 1988, **0925**, 308–316.
49 S. Zhu, S. Wang, L. Yang, T. Huang and X. Yan, *Sci. China: Chem.*, 2011, **54**, 1244–1253.
50 W. Lauterborn, *J. Acoust. Soc. Am.*, 1976, **59**, 283–293.
51 T. Faez, M. Emmer, K. Kooiman, M. Versluis, A. van der Steen and N. de Jong, *IEEE Trans. Ultrason. Ferroelectr. Freq. Control*, 2013, **60**, 7–20.
52 J. E. Hall, *Guyton and Hall Textbook of Medical Physiology*, Elsevier Saunders, Philadelphia, 12th edn, 2010.

53 ANSYS® Academic Research, Release 14.5, Help System, Modeling Discrete Phase, ANSYS, Inc.
54 C. A. Sennoga, J. S. Yeh, J. Alter, E. Stride, P. Nihoyannopoulos, J. M. Seddon, D. O. Haskard, J. V. Hajnal, M.-X. X. Tang and R. J. Eckersley, *Ultrasound Med. Biol.*, 2012, **38**, 834–845.
55 A. Beekman, D. Shan, A. Ali, W. Dai, S. Ward-Smith and M. Goldenberg, *Pharm. Res.*, 2005, **22**, 518–522.